

Application of VTB in design and testing of satellite electrical power systems

Zhenhua Jiang*, Roger A. Dougal, Shengyi Liu

Department of Electrical Engineering, University of South Carolina, Columbia, SC 29208, USA

Received 3 February 2003; accepted 10 February 2003

Abstract

Satellite electrical power systems (SEPS) are strongly interdisciplinary, exhibit complex nonlinear behavior, and operate over a wide range of power levels. The Virtual Test Bed (VTB) provides a unified computational environment that allows rapid modeling, simulation and virtual-prototyping of such complex systems. VTB handles modeling in a comprehensive and efficient way by using both topological and mathematical descriptions. The VTB is also endowed with mechanisms to import models and to co-simulate with other standard software. This paper presents a study of two representative SEPSs to demonstrate design and testing of such systems in the VTB. The performances of Li-ion and Ni–H₂ batteries are compared in a particular system.

© 2003 Elsevier Science B.V. All rights reserved.

Keywords: Battery; Solar array; Satellite electric power system; Shunt regulator; Virtual Test Bed

1. Introduction

A typical satellite electrical power system (SEPS) comprises a primary power source (solar array), an energy storage system (rechargeable batteries such as Ni–Cd, Ni–H₂, or Li-ion, or possibly new technologies such as flywheels), a shunt regulator, a power distribution and control unit (PDCU) and loads, as shown in Fig. 1. It contains components from multiple disciplines such as photovoltaics, electrochemistry, electrical system, control system and power electronics, complex nonlinear behaviors, for example, in the solar array and battery, and a wide range of power levels for power handling and signal processing. Due to the high manufacturing cost and complexity, it is necessary and important to perform simulation studies and build virtual-prototypes for satellite electrical power systems prior

to construction of real hardware. Such prototypes help the engineers optimize the system architecture, components, and the system performance in terms of efficiency, power density, cost and lifetime. Many simulation tools have been proposed to study SEPS including circuit-oriented packages such as SPICE [1,2], PSpice [3], general-purpose state-flow or signal-flow simulators such as MatLab/Simulink [4], EASY5 [5,6] and application-specific software such as EBLOS [7]. Each of these simulation environments favors only one model formulation method, either structural modeling (circuit schematics), or behavioral modeling (mathematical equations). The circuit-oriented approach is intuitive and easy to understand, but in practice, it is often difficult, or even impossible to model a complex system because some parts of the system do not yield to easy expression of their characteristics in terms of existing circuit components. Therefore, it is advantageous to express some models in a mathematical formulation. The best parts of both modeling approaches can be accomplished by using a more integrative environment—the Virtual Test Bed (VTB) [8,9], the philosophy of which is consistent with IEEE standard [10]. VTB allows handling natural power flow, signal and data coupling between devices from multi-disciplines and offers a combination of both topological and mathematical expressions in model formulation for a comprehensive and efficient modeling process. In addition to the powerful capabilities for modeling, the VTB is endowed with mechanisms for

Abbreviations: ACSL, advanced circuit simulation language; BCDC, battery charge/discharge controller; BJT, bipolar junction transistor; DC, direct current; DET, direct energy transfer; EBLOS, energy budget low orbit satellite; HIL, hardware-in-the-loop; Li-Ion, lithium ion battery; MOS-FET, metal-oxide-semiconductor field effect transistor; Ni–Cd, nickel cadmium battery; Ni–H₂, nickel hydrogen battery; PDCU, power distribution and control unit; RC, resistive companion; SEPS, satellite electrical power system; SOC, state of charge; SOD, state of discharge; SPICE, simulation program with integrated-circuit emphasis; VTB, Virtual Test Bed

* Corresponding author. Tel.: +1-803-777-9314; fax: +1-803-777-8045.
E-mail address: jiang@engr.sc.edu (Z. Jiang).

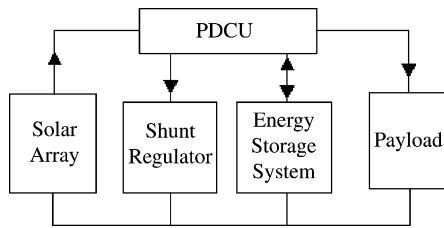


Fig. 1. Block diagram of the satellite electrical power system.

co-simulating with MatLab/Simulink, for importing models from ACSL (including co-simulation), for network-based simulation, and for simulation with hardware-in-the-loop (HIL) [11–13]. Because of these capabilities, VTB can assist in integrating expert knowledge from many disciplines, allowing study of the dynamic behaviors of complex interdisciplinary systems.

Complexity in modeling and simulation arises from satellite electrical power systems for several reasons. (1) The energy conversion and storage devices, such as the solar array and battery, involve multi-physics processes including photoelectric, electro-thermal and electrochemical processes. While conventional simulators are optimized for simulation in specialized disciplines, they are often incapable of dealing with the interdisciplinary modeling in a consistent and convenient manner, and in addition, they have difficulties in tackling strong nonlinearities existing in these devices. (2) The power distribution and control unit, responsible for power distribution and bus voltage regulation, has both devices for power handling and devices for signal processing and control. Using VTB, it is possible to express both the system topology and the component behavior in the most appropriate way (for example, using MatLab/Simulink for signal flow modeling of controllers, ACSL for state-based modeling of dynamic systems, etc.). It is thus easy to build a virtual prototype of the entire system that is suitable for detailed study of the system performance, even when people from different technical areas have contributed to definition of the various components of the system.

The method used in this paper models the interdisciplinary devices in the native VTB format, to designs the control system in Simulink, and then simulates the entire system in the VTB environment by importing the Simulink models. In this paper, interdisciplinary model formulation of various power handling components using native VTB resistive companion (RC) method [14] and model formulation of the regulator and control systems in MatLab/Simulink are presented. A direct energy transfer (DET) system is first studied to investigate the operation and performance of the shunt regulator. An example satellite electrical power system is then assembled using a combination of native and imported models. A simulation study is conducted to investigate the performance of the battery charging/discharging controller. The performances of Li-ion and Ni-H₂ batteries are compared.

2. Native RC modeling of the components

Both natural components and control systems are involved in a SEPS. Natural components, i.e. those to which energy conservation principles apply, are formulated by following the resistive companion approach as described in [14]. The method starts with mathematical expression of the device physics (or process) and yields a discretized set of time-domain linear equations in terms of terminal across and through variables.

The resistive-companion model of a n -terminal device, as illustrated in Fig. 2, described by its across variable vector $V(t)$ and through variable vector $I(t)$, has a standard form as follows:

$$I(t) = G(t-h)V(t) - B(t-h) \quad (1)$$

where $G(t-h)$ is the device conductance matrix, $B(t-h)$ is the through-variable history vector, and

$$G(t-h) = (g_{i,j}(t-h))_{n \times n} \quad (2)$$

$$B(t-h) = -I(t-h) + G(t-2h)V(t-h) \quad (3)$$

where h is the time step size taken by the time-domain solver. The formulation of the equations is not discipline specific, so unlike structural modeling, which tends to be discipline specific, the approach can be applied to physical processes of any discipline.

In the following, solar array, battery system and power converter are modeled here in detail, which are the important energy conversion and conditioning devices in a satellite electrical power system.

2.1. Solar array

The process of converting solar energy into electric energy in a semiconductor solar cell is well known [15–19]. Accompanying the process is heat generation due to direct infrared absorption and ohmic heating. Since the energy conversion process is affected not only by the cell properties and the load condition, but also by the solar irradiance and the temperature, it is necessary to build a multi-physics model [20] involving three energy domains: light, electricity and heat. Fig. 3 shows an equivalent circuit of the solar cell based on consideration of its interactions with its surroundings. The terminals v_0 and v_1 , denoted by their across variables (voltages in V), are electrical in nature and deliver electric energy to the load. The terminal v_2 (or P , the solar

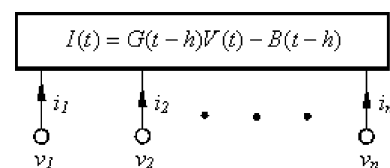


Fig. 2. A device of n terminals described by the resistive companion model.

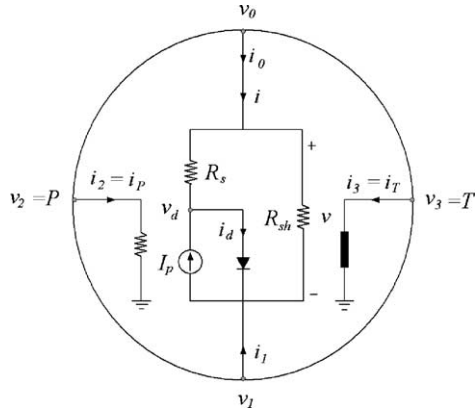


Fig. 3. The equivalent circuit of resistive companion model for photo-voltaic energy conversion by a semiconductor cell.

irradiance on the cell surface in W/m^2) is a light-receiving terminal. And the terminal v_3 (or T , the temperature of the cell in K) is thermal in nature and it conducts heat power to the ambient.

The electrical characteristic of a solar cell can be mathematically expressed as,

$$i(t) = \frac{1}{R_s} \left(v(t) - \gamma v_{\text{th}}(t) \right) \times \ln \left(\frac{I_P(t) + i(t) - (v(t)/R_{\text{sh}})}{I_{\text{sat}}(t)} + 1 \right) + \frac{v(t)}{R_{\text{sh}}} \quad (4)$$

where v and i are the voltage (V) and current (A) at the solar cell terminals, γ is the cell diode ideality factor, and R_s and R_{sh} are the cell body series and shunt resistance (Ω). The thermal potential v_{th} (V), saturation current I_{sat} (A), and the diode current i_d (A) can be expressed, respectively, as

$$v_{\text{th}}(t) = \frac{kT(t)}{e} \quad (5)$$

$$I_{\text{sat}}(t) = I_{\text{sat},0} \left(\frac{T(t)}{T_0} \right)^3 \exp \left(\frac{e}{\gamma k} \left(\frac{E_g(T_0)}{T_0} - \frac{E_g(T(t))}{T(t)} \right) \right) \quad (6)$$

$$i_d(t) = I_{\text{sat}}(t) \left(\exp \left(\frac{v_d(t)}{\gamma v_{\text{th}}(t)} \right) - 1 \right) \quad (7)$$

where k and e are Boltzmann constant and the electronic charge, respectively, T_0 the reference temperature (K), T the cell temperature (K), $I_{\text{sat},0}$ the saturation current at the reference temperature (A), E_g the energy band gap (eV), and v_d the diode voltage (V). The light-induced current (A) is directly proportional to the irradiance, which is given by

$$I_P(t) = \mathfrak{R}AP(t) + C[T(t) - T_0] \frac{P(t)}{P_0} \quad (8)$$

where A is the cell active area (m^2), C the temperature coefficient of light-induced current due to temperature change (A/K), P the irradiance (A/m^2), P_0 the irradiance at the temperature T_0 (A/m^2), and \mathfrak{R} is the spectral-averaged responsivity (A/W).

To construct a natural heat power transport terminal, a thermal current i_T (W/K) is defined such that the product of the temperature and the thermal current equals heat power (W). (Note: We have since changed the way we model thermal systems—we no longer use thermal current as defined here, but instead we use heat power as the through variable, which is more conventional.) The heat transported through the thermal terminal is characterized by the energy balance equation, as given by following equation [20]:

$$c_p M \frac{dT(t)}{dt} = \frac{[v(t) - v_d(t)]^2}{R_s} + \frac{[v(t)]^2}{R_{\text{sh}}} + i_d(t)v_d(t) + (1 - \rho - \tau - \eta)AP(t) + i_T T \quad (9)$$

where c_p is the averaged specific heat (J/kg/K), M the averaged mass (kg), the symbols ρ , τ , and η denote the reflection coefficient, transmission coefficient and quantum efficiency of the cell, respectively. Eq. (9) explains that the energy absorbed by the cell (resulting in temperature increase) is due to the heating by electro-thermal processes (the first three terms on the right-hand side), direct absorption (the fourth term) and heat exchange with connected structures (the last term).

The standard RC equations as shown in Eqs. (1)–(3) can then be derived for solar array model based on Eqs. (4)–(9). Note that this model is a general model based on the physics of solar array. A specific solar array can be modeled by changing the model parameters. In order to validate this model, the simulated i – v characteristic for a particular solar cell is compared with the experiment data. The experiment was performed for a 0.5 cm^2 copper indium diselenide (CuInSe_2) thin film solar cell [19] at an irradiance of 1000 W/m^2 and at 25°C [21]. The air mass is 1.5 and fill factor the solar cell is 64.27%. The measured i – v characteristic is given in Fig. 4. Also plotted in Fig. 4 are the simulated i – v curves at 15, 25, and 35°C , respectively. The same irradiance and solar cell parameters are used in the simulation. From Fig. 4, it is clear that the simulation result agrees well with the experiment data at 25°C . It is also seen that the open circuit voltage decreases with the temperature while the short circuit current increases with the temperature.

2.2. Battery energy storage system

Energies in battery systems take chemical, electrical and thermal forms. Internally, the battery converts chemical energy into electrical energy during discharge (the reverse during charge), and it generates heat due to both irreversible processes (e.g. ohmic heating) and reversible processes (entropy change). Externally, the battery interacts with its surroundings both electrically (delivering electric power via the electrical terminals) and thermally (transporting heat through its surface). Here, we use Ni– H_2 battery to illustrate modeling of the electrochemical and thermal processes involved in a battery system.

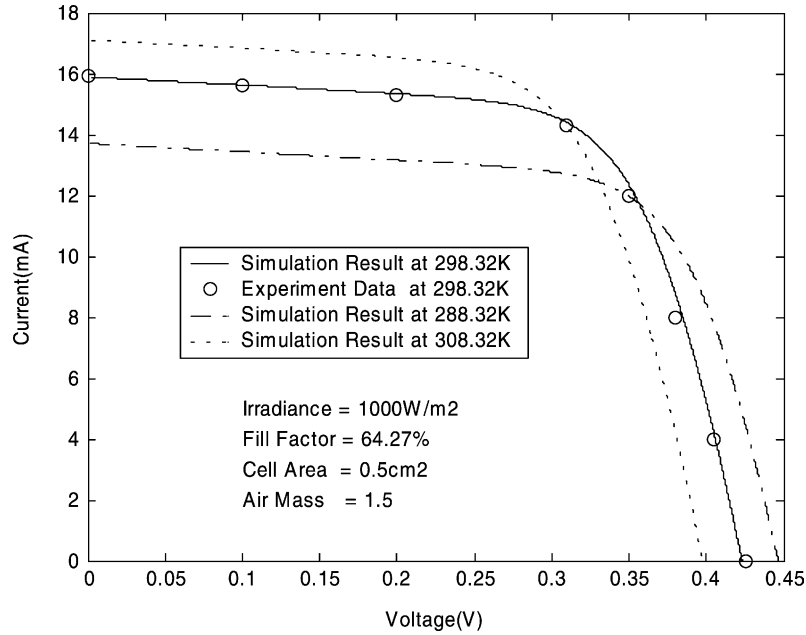


Fig. 4. Comparison of the simulated and experimental $i-v$ characteristics.

Several detailed Ni–H₂ battery models have been published, among which the model of Wu and White [22,23] and Weidner and coworkers [24] includes considerable details of the electrochemical kinetics and thermodynamics. VTB allows to capture their expertise in the electrochemical discipline by integrating their battery models in the VTB environment for system studies. The Ni–H₂ battery model presented here results from collaboration with these authors. The present model is somewhat simplified, but it still captures the major features of Ni–H₂ characteristics. In the model, only two reactions are considered: the nickel reduction/oxidation at the positive electrode, which is a decisive reaction for the battery potentials; and the water oxidation (or oxygen evolution), which dominates the over-charge process. Hydrogen reaction at the platinum electrode, intermediate reactions and side reactions are ignored. In addition, the kinetics of reactions are ignored (assumed instantaneous).

The overall reversible potential, $E_{\text{Ni}}(T, x)$, corresponding to the nickel reaction, and the resulting current from the oxygen reaction, $i_{\text{O}_2}(T)$, are determined by Eqs. (10) and (11):

$$E_{\text{Ni}}(T, x) = E_{\text{Ni}}^0(T) + \frac{RT}{F} \ln \left(\frac{1-x}{x} \right) + \frac{RT}{2F} [A_0(T)C(x) + B_0(T)D(x)] \quad (10)$$

$$i_{\text{O}_2}(v, T) = AL_+ ai_{\text{O}_2}(T) \times \exp \left[4(1 - \alpha_{\text{O}_2}) \frac{F}{RT} (v - E_{\text{O}_2}(T)) \right] \quad (11)$$

where R is the gas constant (8.314 J/mol/K), F the Faraday constant (96,485 coulombs/mol), x and T are state of discharge and temperature of the battery, both of which are

functions of time, E_{Ni}^0 , A_0 and B_0 are functions of temperature only, and C and D are functions of the state of discharge only, A and L_+ are the electrode area and thickness, respectively, α_{O_2} is the transfer coefficient for oxygen reaction, v the battery terminal voltage (V), E_{O_2} the reaction potential (V), a the specific area (m²/m³) of the electrode, and $i_{\text{O}_2,0}$ the exchange current density (A/m²).

The state of discharge, at any instant time t , is determined by the available active material in the battery. It can be conveniently related to the nickel reaction current i_{Ni} as,

$$\frac{dx}{dt} = -\frac{i_{\text{Ni}}}{Q_{\text{max}}} \quad (12)$$

where Q_{max} is the maximum charge stored in the battery for a given capacity (C). In addition, the battery terminal voltage can be related to the current, considering internal potential losses, as,

$$v = E_{\text{Ni}} + R_i i_{\text{Ni}} \quad (13)$$

where R_i (Ω) is a fitting parameter representing overall internal resistance due to ohmic, surface kinetic and concentration limitation losses.

The heat energy in the battery is characterized by the energy balance equation given in Eq. (14):

$$c_p m \frac{dT}{dt} = i_{\text{Ni}} \left(v - E_{\text{Ni}} + T \frac{\partial E_{\text{Ni}}}{\partial T} \right) + i_{\text{O}_2} \left(v - E_{\text{O}_2} + T \frac{\partial E_{\text{O}_2}}{\partial T} \right) + i_{\text{T}} T \quad (14)$$

where m is the battery mass (kg) and c_p the average specific heat (J/kg/K). Notice that heat terms include both resistive and reversible ones. The last term on the right-hand side

is the heat transported to the surroundings due to cooling mechanisms. Again, the thermal current i_T represents heat flow out of the thermal terminal, which can be separately described by any one or more mechanisms such as conduction, convection, or radiation.

The pressure inside the Ni–H₂ battery vessel is an indicator of the state of discharge of the battery and of the battery potential. A sensor is usually built inside the battery to detect the pressure for the purpose of protecting against battery overcharge. According to the ideal gas law, the pressure P (Pa), and the nickel and oxygen reaction currents $i_{Ni}(T)$ and $i_{O_2}(T)$ can be related by the following equations:

$$P(t) = \frac{[n_{H_2}(t) + n_{O_2}(t)] RT(t)}{V_g} \quad (15)$$

$$i_{Ni}(t) = 2F \frac{dn_{H_2}(t)}{dt} \quad (16)$$

$$i_{O_2}(t) = 4F \frac{dn_{O_2}(t)}{dt} \quad (17)$$

where n_{H_2} and n_{O_2} are the mole numbers of hydrogen and oxygen (mol). Notice that in writing Eq. (16), we assume that the nickel reaction current is equal to the hydrogen reaction current.

Fig. 5 shows the icon for the Ni–H₂ battery in VTB schematic view. Behind the icon is the battery physics described by Eqs. (10)–(17) as reduced to resistive companion form. Notice that the pressure terminal is a signal terminal since there is no mass transport through the battery vessel. The details of Ni–H₂ battery model can be found in [25] and it is also validated by the experiment data.

2.3. Power converter

In a SEPS, the battery is charged through a buck converter, which is controlled by a battery charge/discharge controller (BCDC) by dynamically monitoring the voltage, current and temperature of the battery. The simplified circuit of the battery charger is illustrated in Fig. 6. The power converter parameters and variable definitions are also shown in this figure. When choosing the output capacitor voltage v_o and inductor current i_L as the state variables, the time-averaged model of the buck converter is given by

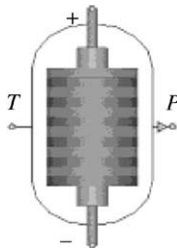


Fig. 5. VTB schematic view of the Ni–H₂ battery. Anode and cathode are electrical terminals: T is the thermal terminal and P is the pressure signal terminal.

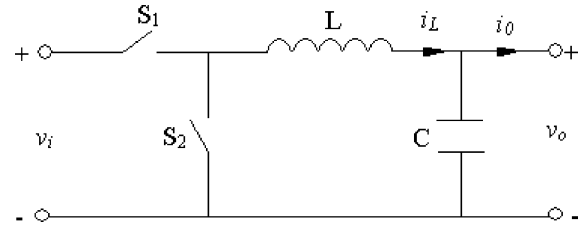


Fig. 6. Illustration of the battery charger.

$$C \frac{dv_o}{dt} = i_L - i_o \quad (18)$$

$$L \frac{di_L}{dt} = dv_i - v_o \quad (19)$$

where d is the duty cycle used to control the switching of the converter, v_i the power source voltage, L and C are the inductance and capacitance of the output filter, and i_o is the output current.

Since the goal of the system level simulation is to investigate the energy balance in the electrical power system and to monitor the main parameters of the system, the simulation time step can be long, for example, higher than 1 s. In this case, an average-value model of the converter is used and the switching transients are not resolved. The power flow in the converter is controlled by adjusting the average on/off duty cycle of the switching. The average output voltage of the buck converter is determined by the following equation:

$$\frac{V_o}{V_i} = \frac{t_{on}}{T} = d \quad (20)$$

where V_i and V_o are the average input and output voltages of the converter, respectively, t_{on} is the turn-on time of the switch during a period and T the switching period.

2.4. Other components

The radiator cooling mechanism is modeled based on the radiation law, which is equivalent to a “temperature transformer” transporting heat power from a primary side to a second side. Heat carried away through the radiator follows the blackbody radiation law. The thermal across and through variables are defined as temperature and thermal current for natural thermal coupling and heat transport. The irradiance model computes the illumination of the solar array based on the date/time and the orbital parameters of the satellite. The user can select between low earth orbit and geo-synchronous orbit. The model can output Earth position, Earth rotation, and the position of the satellite for use in the visualization system.

Also included in the studied systems are models for conventional components such as sensor, resistor and capacitor, which are not described in detail here.

3. Control system design

In this paper, the controller or regulator is designed in Simulink and then imported to VTB for system simulation. For the VTB–Simulink interface, the input ports are modeled as infinite impedance ports and the output ports are zero impedance ports. This assumption is reasonable when the interconnection is between a circuit and a controller: an input port for the Simulink model will generally convey a measured value (for example, the sampled voltage) while the output will usually be a control variable. In this case, from the point of view of the VTB solver, a new multi-port element can be defined for the Simulink model. At every time step, the measured variables are input to the Simulink model through the VTB–Simulink interface. The control variables are calculated in the Simulink model and then output to VTB. Models of solar array shunt regulator and battery charge/discharge controller are discussed in detail later.

3.1. Shunt regulator

Shunt regulators are used in SEPSs to limit the power bus voltage by dissipating the excess solar array power. They can be implemented with many technologies, such as sequential shunt system, partial shunt system, digital shunt system, etc. [26–29]. A sequential shunt regulator, which selects the number of solar array sections needed to both supply the load and to enable the batteries to be charged in a desired manner and switches in or out solar array section sequentially, is modeled here as an example. Each shunt can be implemented either by a MOSFET switch in series with a shunt resistor, or by an MOSFET driven BJT pair where the BJT pair acts as the dissipative element and the ohmic heating is generated mainly in the bipolar transistor, or other combinations. Here we use the former implementation, which is modeled as an ideal switch in series with a dissipative resistor. Fig. 7 shows the Simulink model of a sequential shunt regulator for four solar array sections. The shunt regulator model produces four switching signals, S1, S2, S3, and S4, for the shunt elements by comparing the bus voltage with the

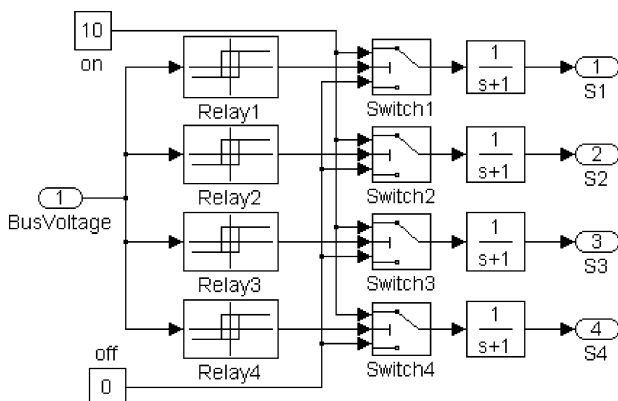


Fig. 7. Simulink diagram of sequential shunt regulator model.

four pairs of upper and lower voltage setpoints, which are user-defined. When the bus voltage exceeds an upper limit, the corresponding switching signal is ‘on’ and the solar array section is shunted. When the bus voltage drops below the lower limit, an ‘off’ switching signal is produced to deactivate the corresponding shunt element. This Simulink model can be used in either of two ways. First, when the controller is still in development, the Simulink model can be used in an interactive co-simulation mode that allows adjustment of the controller parameters during system simulation. Second, once the controller design has been finalized, the controller model can be compiled into an executable that allows others to study the system behavior without having to actually run MatLab or Simulink.

In general, for a battery energy storage system, a desired voltage level can be obtained by connecting a string of battery cells in series, but charge mismatch may occur due to minor differences among the cells. To overcome the mismatch, a shunt regulator that is implemented as voltage-controlled switch with hysteresis, can be used for each battery cell to equalize charge and match SOC of the battery. When the battery voltage exceeds a preset level, the resistor is connected in parallel to the battery terminals. The battery discharges through the shunt resistor and the voltage decreases. When the battery voltage drops below another predetermined value (or reactivated voltage), the shunt branch is disconnected.

3.2. Battery charge/discharge controller

In this paper, the battery charge controller follows a constant current charging/constant voltage floating regimen, and the reference voltage is temperature compensated. Both current control and voltage control are implemented through proportional control strategy. The control scheme can be formulated as follows:

$$V_{\text{ref}} = V_{\text{ref},0} - C_T(T - 293.32) \quad (21)$$

$$d = d_{\text{old}} + k_i(I_{\text{ref}} - I), \quad \text{if } V < 0.98 \times V_{\text{ref}} \quad (22)$$

$$d = d_{\text{old}} + k_v(V_{\text{ref}} - V), \quad \text{if } V \geq 0.98 \times V_{\text{ref}} \quad (23)$$

where V , I , T are the sampled voltage, current, and temperature of the battery, respectively, d and d_{old} are the current and previous duty ratios used to control the buck converter, $V_{\text{ref},0}$ and I_{ref} are the desired voltage and charging current of the battery at 293.32 K, C_T is the temperature coefficient with respect to the voltage, k_i and k_v are current gain and voltage gain, respectively.

The Simulink model for the BCDC is shown in Fig. 8. Three input terminals are for the sampled voltage, current, and temperature of the battery, respectively. The output duty ratio is obtained from either the voltage-control loop or the current-control loop, depending on the battery voltage. An output memory mechanism guarantees the smooth change between these two control schemes. The switching signal

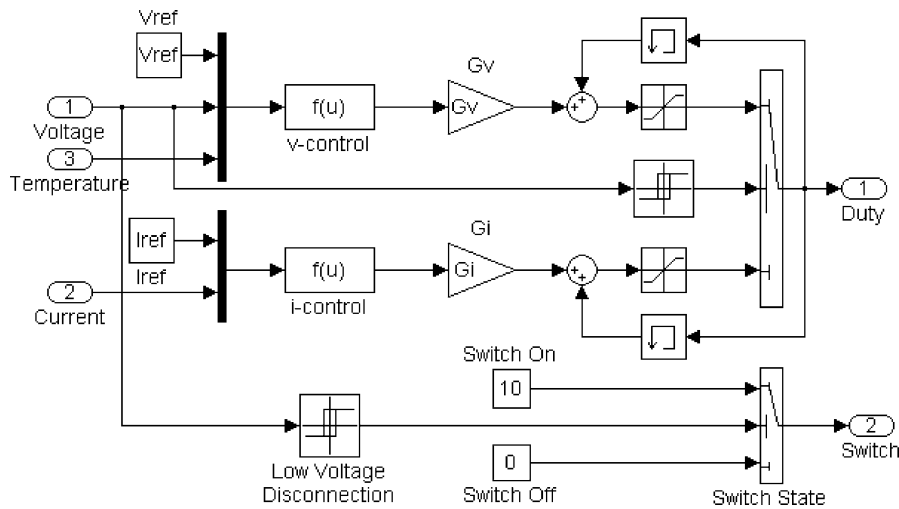


Fig. 8. Simulink diagram of battery charge/discharge controller model.

terminal is used to manage the discharging of the battery. When the monitoring voltage is below a preset value (or low voltage disconnection setpoint), the controller can output a signal to disconnect the loads in order to protect the battery from over discharging. A hysteresis allows reconnecting the loads when the battery voltage increases to an acceptable level.

4. Results and discussion

4.1. Bus voltage regulation

In order to investigate the operation and performance of the sequential shunt regulator and battery shunt, a direct energy transfer (DET) power system, as shown in

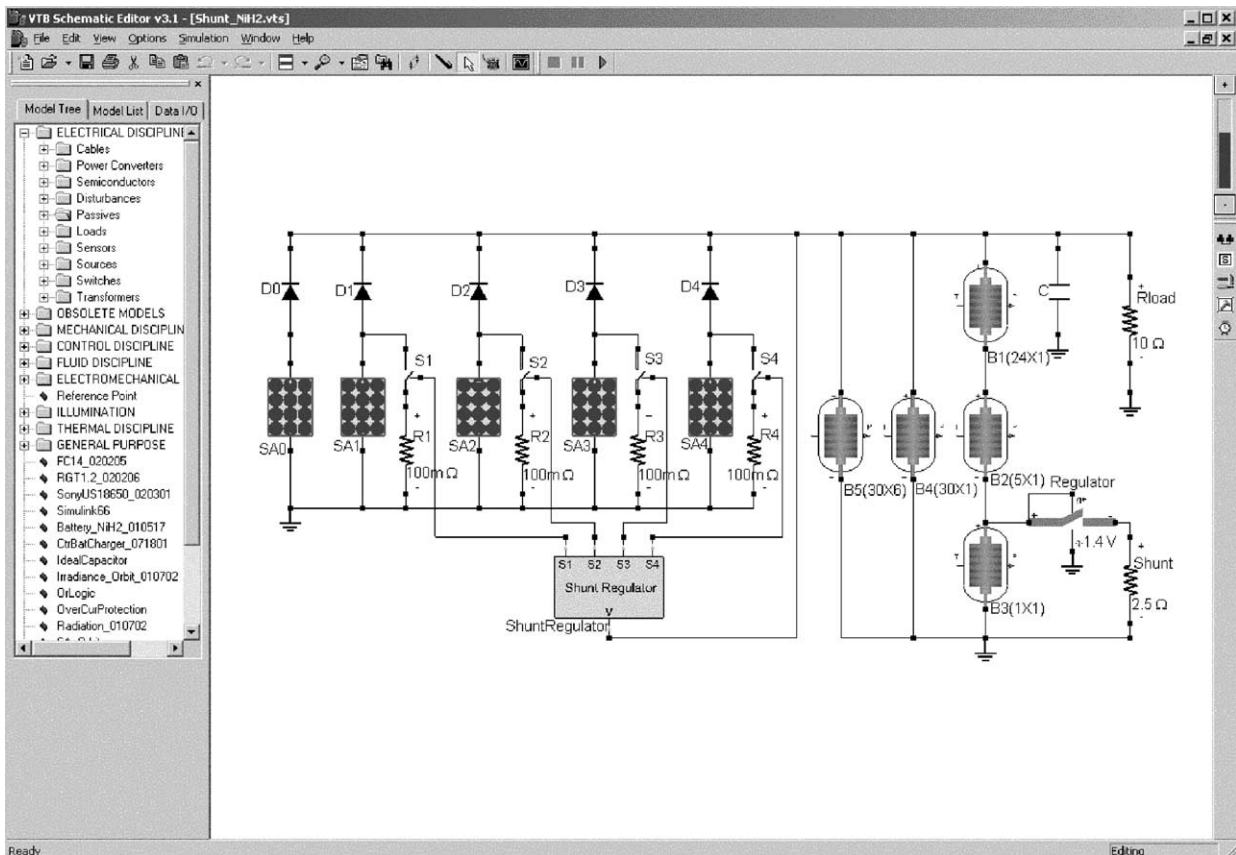


Fig. 9. Schematic diagram of a simplified DET satellite electrical power system.

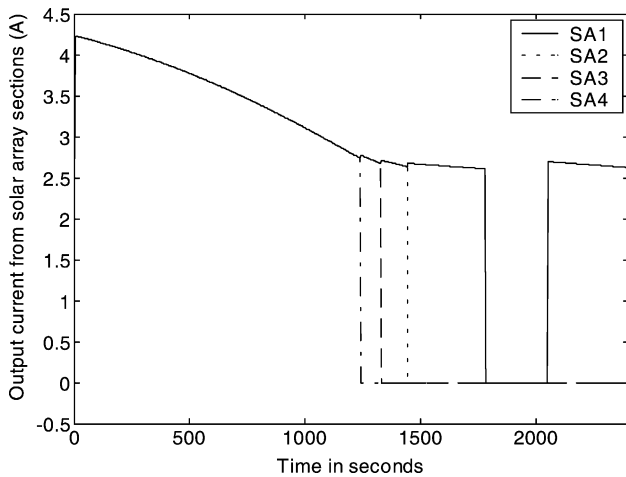


Fig. 10. Output currents from four solar array sections: SA1 (line), SA2 (dot), SA3 (dash), and SA4 (dash-dot).

Fig. 9, is studied. Four solar array strings: SA1–SA4, are sequentially shunted array sections, which performs coarse regulation of the bus voltage. An active array section, SA0, which is directly connected to the main bus without shunt, is responsible for fine regulation of the bus voltage. Each section is individually switched in or out depending on the bus voltage and the switching reference voltages except the active section, which is connected to the bus all the time. A sequential shunt regulator controls the switching of four shunt elements. It is compiled from Simulink model and imported to VTB. The upper voltage setpoints of the regulator for solar array sections SA1–SA4 are 41.50, 41.48, 41.45, and 41.40 V, respectively. The lower setpoints are 41.4, 41.2, 41.1, and 41.0 V, respectively.

Each solar array section is an 88×2 array (series connections by parallel connections). The Ni–H₂ battery is nominally an array of 30×8 cells, but in the simulation model two individual series strings are split out for more detailed study, and in one of those strings, an individual cell is re-

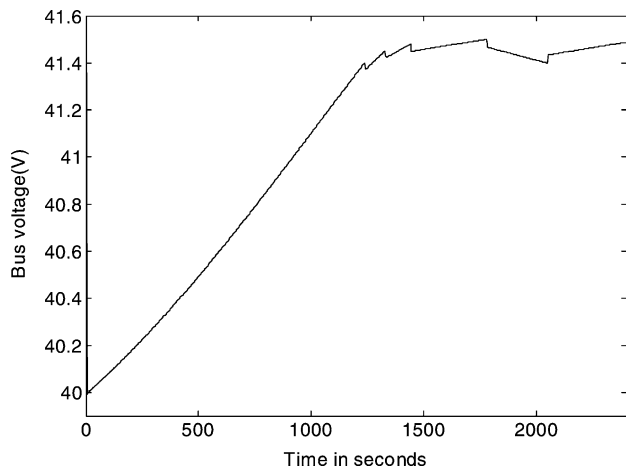


Fig. 11. Simulation result of the bus voltage.

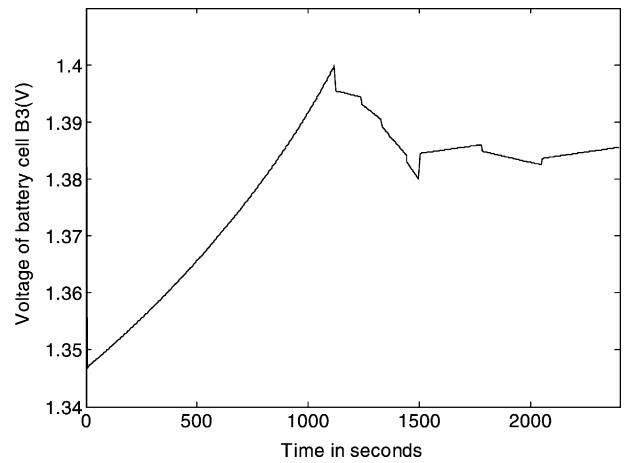


Fig. 12. Voltage of battery cell B3.

vealed. Accordingly, the numbers of series and parallel cells are (24×1) , (5×1) , (1×1) , (30×1) , (30×6) , respectively for B1–B5. The initial state of charge (SOC) of B3 cell is 0.70 while those of all the others are 0.60. The load is a resistor of 10Ω . A filter capacitor connected to the main bus is used to smooth the bus voltage. The resistance of the shunt resistor for a solar array section is chosen as 0.1Ω , and then a shunt element that can bear more than 10 W ohmic heat is needed since the short-circuit current of a solar array section is about 9.5 A. To prevent an individual battery cell from overcharging, the turn-on voltage of the battery shunt is set to 1.4 V and the reactivated voltage is 1.38 V. The resistance of the shunt element is chosen as 2.5Ω , through which about 550 mA current will conduct when the battery is shunted. In this case, power of about 0.8 W is dissipated in each battery shunt. For convenience, only one battery shunt is shown in Fig. 9.

Simulation is conducted for the first 40 min of the orbit cycle, and the results are given in Figs. 10–13. Fig. 10 shows the output current from four shunted solar array sections,

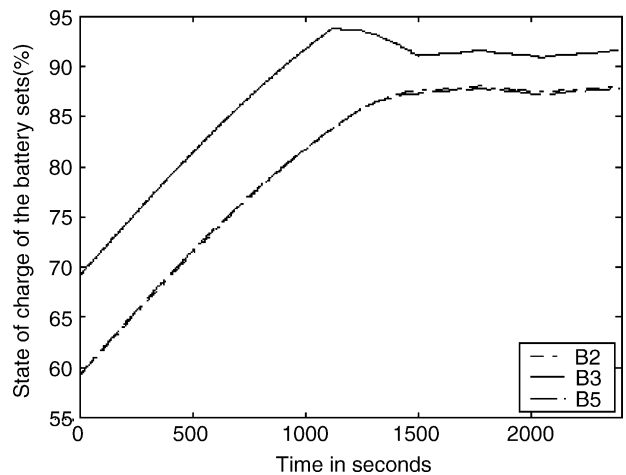


Fig. 13. States of charge of three battery sets: B2 (dash), B3 (line), and B5 (dash-dot).

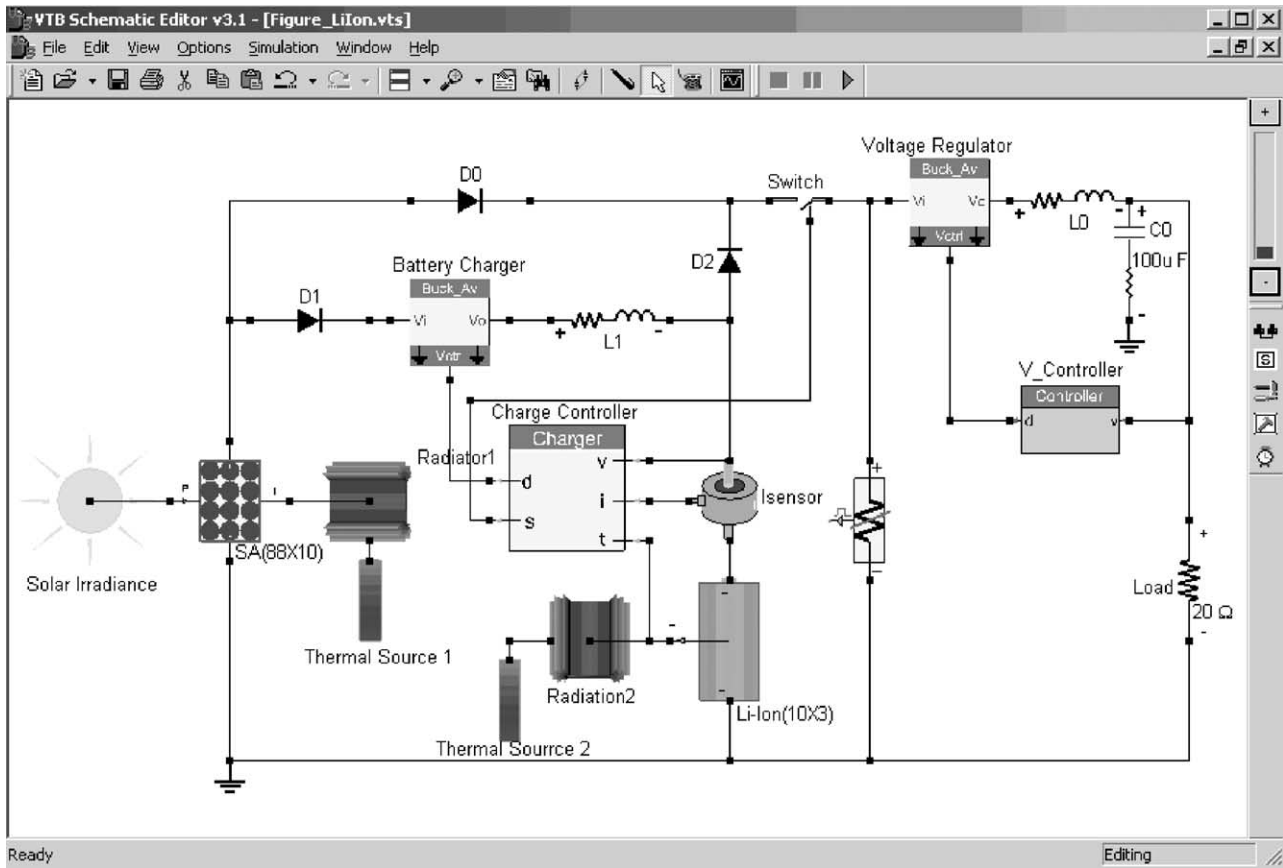


Fig. 14. Schematic view of example satellite electrical power system.

which contribute to load requirement and battery charging. Note that each of them is not the actual current through the solar array, but the current through the blocking diode or the current that is not shunted. Fig. 11 shows the bus voltage, which increases initially from 40.0 V. From Figs. 10 and 11, it can be seen that when the bus voltage arrives at the 41.40 V setpoint of the shunt regulator, solar array

SA4 is first shunted, and the output current from this section becomes zero. Then the remaining four solar array sections, including the active section, provide power for the batteries and load. There is a fast but small amplitude decrease in bus voltage and afterwards the bus voltage increases. The solar

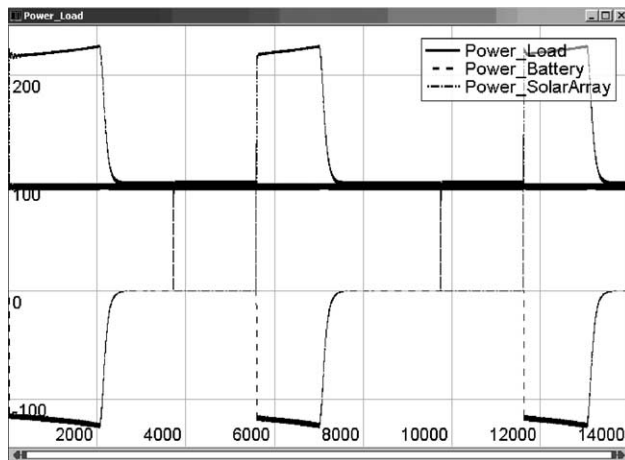


Fig. 15. Power profiles of solar array (dash-dot), Li-Ion (dash), and loads (solid line).

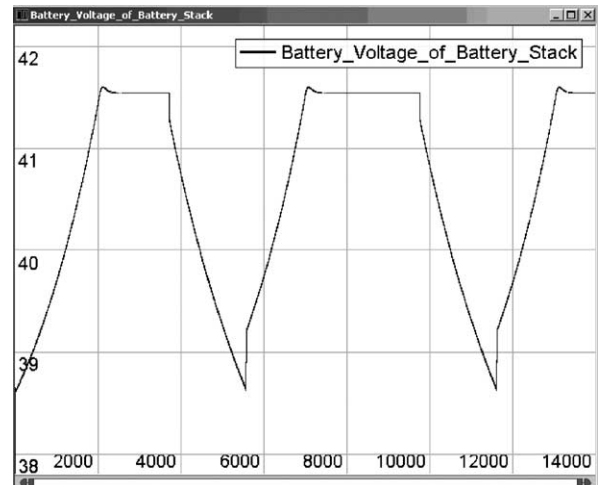


Fig. 16. Li-Ion voltage. The battery voltage increases from 38.7 V. After about 2000 s of 3 A charging, it arrives at the preset point and thereafter floats at that value. The voltage decreases to about 38.7 V during the discharge cycle.

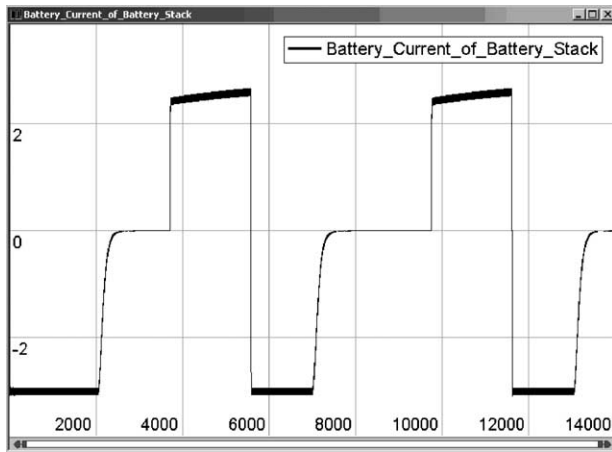


Fig. 17. Li-Ion current. The battery is initially charged at 3 A current. After the battery voltage arrives at the reference value, the battery current tapers immediately. The discharge current is about 2.3 A.

arrays SA3, SA2, and SA1 are sequentially shunted when the bus voltage arrives at their setpoints. After four sections are shunted, the bus voltage will decrease continuously because the active section can not support the load and the batteries begin to discharge. When the bus voltage decreases below 41.4 V, section SA1 is activated again.

Due to the differences in initial SOC of the batteries, the battery cell voltages are different. The voltage of battery cell B3 increases faster than the others and it arrives at the upper limit setpoint first. Fig. 12 shows the voltage of cell B3. From Fig. 12, it is clear that when the voltage of cell B3 exceeds 1.4 V, the shunt is activated. Then this battery discharges and the voltage decreases. When the battery voltage drops below 1.38 V, the shunt is deactivated and the battery is charged again. The difference of the state of charge of batteries B2, B3, and B5 is shown in Fig. 13. The SOC of B3 is the highest, and the other two are close. From Fig. 13, it is seen that the increase of state of charge of B3 is slowed down due to the shunt at about 1100 s. From this study, it can be seen that

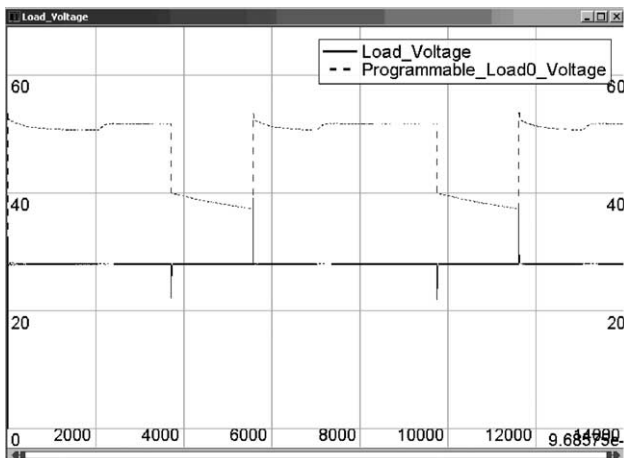


Fig. 18. The regulated and unregulated bus voltages.

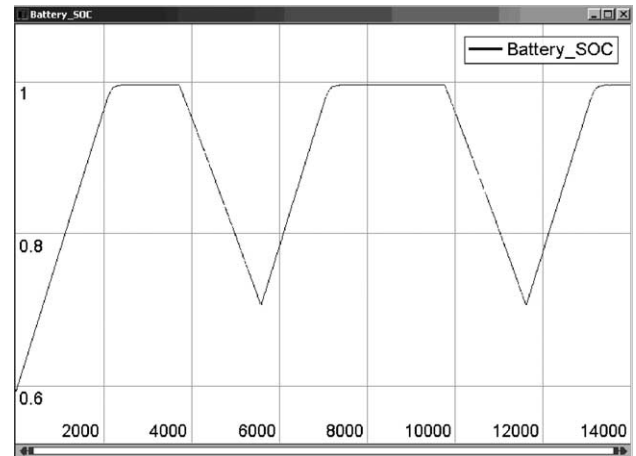


Fig. 19. State of charge of Li-Ion.

the sequential shunt regulator can maintain the bus voltage at a relatively constant level and battery shunt contributes to charge equalization.

4.2. Battery charging/discharging control

A wide variety of systems can be easily configured and simulated based on the native and imported models available in the VTB. A representative SEPS is described in this section, while different systems can be obtained by changing the system topology and the parameters of components. The studied system is assembled in VTB, as shown in Fig. 14, which comprises a solar irradiance model to illuminate the solar cells, a solar array to convert the solar illumination into electrical power, a lithium ion battery (Li-Ion) array, a resistive load, and a pulsed power load. Several auxiliary components in the system are responsible for appropriate and efficient operation of the entire system. The primary energy conversion device is an 88×10 (series by parallel connections) array of single junction silicon cells. Each cell has an active area of $2.4 \text{ cm} \times 6.6 \text{ cm}$, and a responsivity of 0.35 A/W . The battery is a 10×3 array of Li-Ion cells, each

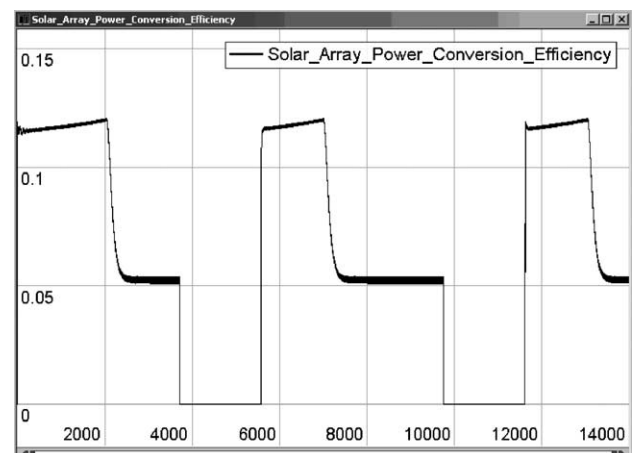


Fig. 20. Energy conversion efficiency of solar array.

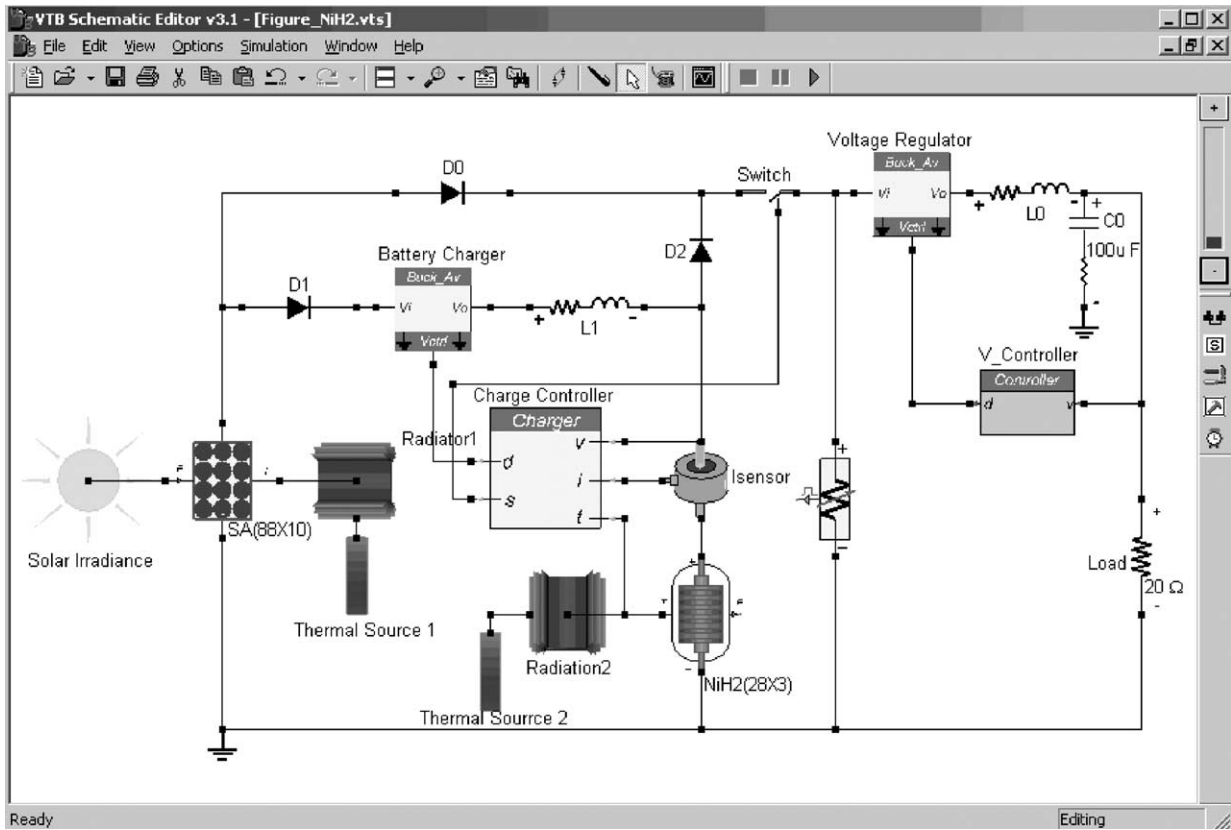


Fig. 21. Schematic of the spacecraft electrical power system with Ni–H₂ battery.

having a nominal voltage of 4.15 V and a capacity of 1.5 Ah. The initial state of charge of the battery is 0.6. All the solar array cells and all the battery cells are lumped into a single model for this particular orbital simulation. Shunts for solar arrays are not included in this system. The charge controller is compiled from the Simulink model and imported to VTB.

The pulsed power load consists of a 55 W constant power load and a 5 W pulse power load which is active once every second. Another load is a 20 Ω resistive load, which is connected to a 28 V regulated voltage bus. The charging current reference and floating voltage reference for the battery charge controller are 3 A and 41.5 V, respectively.

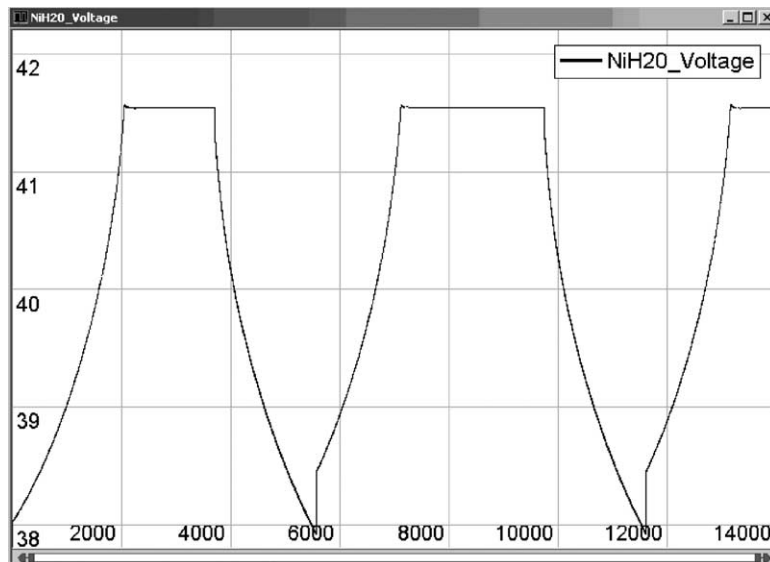


Fig. 22. Ni–H₂ battery voltage.

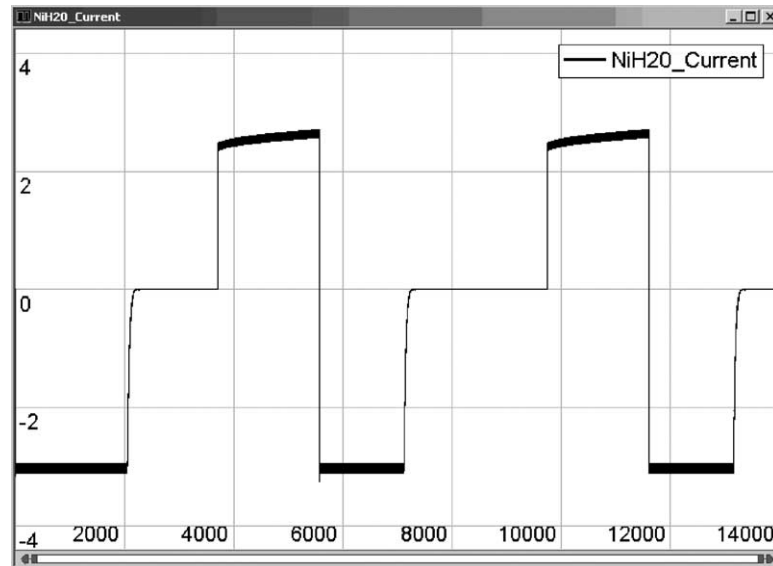


Fig. 23. Ni-H₂ battery current.

This system is simulated for the first 14 ks of the mission, and the calculated results for this system are shown in Figs. 15–20. The time axis in these figures is scaled in seconds and the time step for simulation is 100 ms. Fig. 15 shows the power profiles of the solar array, Li-Ion and loads. As can be seen, when the solar array is in light, it provides power for the loads, charging the battery simultaneously. The power from the solar array is the sum of the load power and the power to the battery. During eclipse, the battery provides power for the loads, and the bus voltage decreases from a value approximately equal to solar array voltage to the battery voltage, which is shown in Fig. 18. The power dissipated by the resistive load does not change with the bus voltage since its voltage is regulated. After a cy-

cle, the solar array powers the loads and charges the battery again.

Figs. 16 and 17 show the sampled data for the voltage and current of the lithium ion battery, respectively. The battery is initially charged at 3 A current, and the charge current has small ripples due to the pulsed power load. After about 2000 s of constant current charging, the battery voltage arrives at the preset point and thereafter it floats at that voltage. Actually, the voltage reference is a little higher than 41.5 V because the battery temperature at this time is lower than the reference value that is set on the ground. When the charging operation moves to constant voltage mode, the charging current tapers immediately. When the solar array goes into eclipse, the battery begins to discharge. As a result,

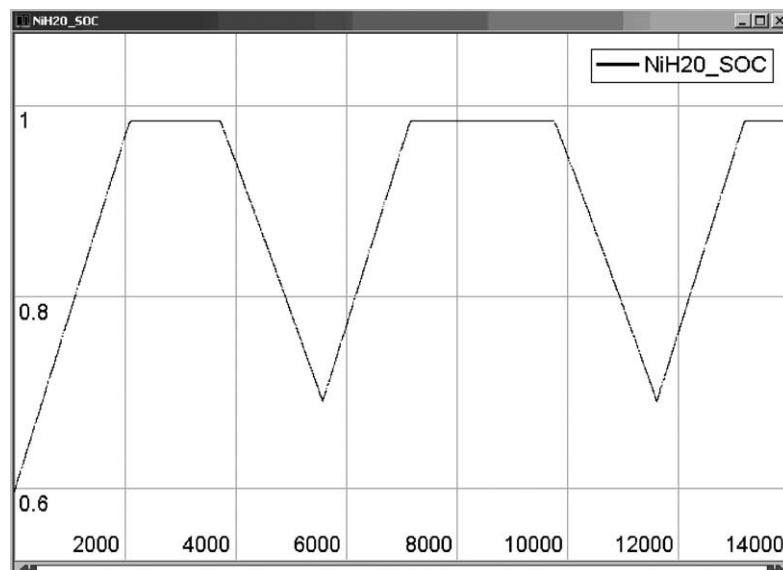


Fig. 24. State of charge of Ni-H₂ battery.

the battery current reverses and its voltage decreases. The discharge current is not controlled and depends on the loads. It is seen from Fig. 17 that the discharging current is about 2.3 A. At the end of the discharge cycle, the battery voltage decreases to about 38.7 V. It is clear from these two figures that the charge controller performs the constant current charging/constant voltage floating scheme correctly.

Fig. 19 illustrates the calculated state of charge of the battery, which increases initially from 0.6 and approaches to 1.0 when it is fully charged. The SOC decreases to 0.7 at the end of discharging. After the first cycle, the SOC changes between 0.7 and 1.0. From this figure, it is seen that the capacity of the chosen battery meets the load power requirement.

Fig. 20 gives the energy conversion efficiency of the solar array, which is about 12% when it powers the battery and loads simultaneously. It is shown that the efficiency declines as the output current decreases because the output power decreases.

Based on the above proposed SEPS system, a different system which replaces Li-Ion battery with Ni–H₂ battery, as shown in Fig. 21, is easily configured in the VTB. In order for the charging control circuit to be applicable, a 28 × 3 array of Ni–H₂ cells with the same capacity as Li-Ion is used. The simulation results are shown in Figs. 22–24. It is seen that the battery charger and control circuit is suitable for Ni–H₂ battery while the series cell number should be adjusted according to the reference voltage. From the simulation results, differences are observed that the current of Ni–H₂ battery tapers to zero more rapidly than Li-Ion during constant voltage control mode and that the voltage of Ni–H₂ drops to 38 V at the end of discharging cycle, a little lower than that of Li-Ion.

5. Conclusions

In this paper, interdisciplinary models for the solar array battery system, power converter, orbit, radiator, and other components have been developed in native VTB RC form. The control systems such as shunt regulator and battery charge/discharge controller have been modeled in MatLab/Simulink and then imported into the VTB.

Based on the native and imported models, two case studies were performed. A direct energy transfer system was simulated to study in detail the operation and performance of the sequential shunt regulator and battery shunt. With the sequential shunt regulator, the bus voltage can be maintained at a relatively constant level. The battery shunt has a capability of equalizing charge of mismatched battery cells. The developed models were then integrated into a representative satellite electrical power system and simulated for a one-orbit cycle. The behaviors of the solar array and battery were studied in detail. The performances of Li-Ion and Ni–H₂ batteries are compared in this example system. It can be seen from the simulation results that the proposed sys-

tem configuration and parameters can meet the system requirements and that the proposed battery charge controller performs the constant current/constant voltage strategy correctly. From the comparison study, it was shown that the battery charger and control circuit is also suitable for Ni–H₂ battery while the series cell number should be adjusted according to the reference voltage.

Acknowledgements

The work described in this paper was supported by MRJ/Veridian, under contract 00-MRJ-1085-100, and by the NRO under contract National Reconnaissance Office-00-C-0134. The Virtual Test Bed is developed under funding from the US Office of Naval Research, under grant #N14000-00-1-0131 and is freely available at <http://vtb.engr.sc.edu>.

References

- [1] R.M. Nelms, B.W. Evans, L.L. Grigsby, Simulation of AC spacecraft power systems, *IEEE Trans. Ind. Electron.* 36 (3) (1989) 398–402.
- [2] R.M. Nelms, L.L. Grigsby, Simulation of DC spacecraft power systems, *IEEE Trans. Aerospace Electron. Syst.* 25 (1) (1989) 90–956.
- [3] W. Billerbeck, G. Lewis Jr., Spacecraft power system studies using PSpice, in: *Proceedings of the 36th Intersociety Energy Conversion Engineering Conference*, vol. 1, 2001, pp. 1–18.
- [4] G. Colombo, U. Grasselli, A. Deluca, A. Spizzichino, Satellite power system simulation, *Acta Astronaut.* 40 (1) (1997) 41–49.
- [5] B.H. Cho, F.C.Y. Lee, Modeling and analysis of spacecraft power systems, *IEEE Trans. Power Electron.* 3 (1) (1988) 44–54.
- [6] J.R. Lee, B.H. Cho, S.J. Kim, F.C. Lee, Modeling and simulation of spacecraft power systems, *IEEE Trans. Aerospace Electron. Syst.* 24 (3) (1988) 295–304.
- [7] A. Capel, J. Ferrante, J. Cornett, P. Leblanc, Power system simulation for low orbit spacecraft: the EBLOS computer program, in: *Proceeding of the IEEE Power Electronics Specialist Conference*, 1982, pp. 272–285.
- [8] R.A. Dougal, C.W. Brice, R.O. Pettus, G. Cokkinides, A.P.S. Meliopoulos, Virtual prototyping of PCIM systems—the Virtual Test Bed, in: *Proceedings of the PCIM/HFPC '98 Conference*, Santa Clara, CA, November 1998, pp. 226–234.
- [9] A.P. Sakis Meliopoulos, G. Cokkinides, B. Beker, R.A. Dougal, A new tool for visualization and animation of power component and system operation, in: *Proceedings of the 33rd Hawaii International Conference on System Sciences*, January 2000.
- [10] VHDL Analog and Mixed-Signal Extensions, *IEEE Standards* 1076.1-1999, March 1999.
- [11] W. McKay, A. Monti, E. Santi, R.A. Dougal, A co-simulation approach for ACSL-based models, in: *Proceedings of the Huntsville Simulation Conference*, Huntsville, AL, October 3–4, 2001.
- [12] R.A. Dougal, T. Lovett, A. Monti, E. Santi, A multilanguage environment for interactive simulation and development of controls for power electronics, in: *Proceedings of the IEEE Power Electronics Specialists Conference*, Vancouver, Canada, 17–22 June 2001.
- [13] V. Dmitriev-Zdorov, R.A. Dougal, N. Merejin, V. Popov, E. Solodovnik, Hardware in the loop simulation of energy systems in the VTB environment, in: *Proceedings of the 5th IASTED International Conference on Power and Energy Systems (PES 2001)*, Tampa, FL, November 19–22, 2001.
- [14] D.A. Calahan, *Computer-Aided Network Design*, revised ed., McGraw-Hill, New York, 1972.

- [15] M.B. Prince, Silicon solar energy converters, *J. Appl. Phys.* 26 (1955) 534–540.
- [16] P. Rappaport, J.J. Loferski, E.G. Linder, The electron-voltaic effect in germanium and silicon p–n junctions, *RCA Rev.* 17 (1956) 100–128.
- [17] J.J. Loferski, Theoretical considerations governing the choice of the optimum semiconductor for photovoltaic solar energy conversion, *J. Appl. Phys.* 27 (1956) 777–784.
- [18] P. Rappaport, The photovoltaic effect and its utilization, *RCA Rev.* 20 (1959) 373–397.
- [19] J. Tringe, J. Merrill, K. Reinhart, developments in thin-film photovoltaics for space, in: *Proceedings of the Twenty-Eighth IEEE Photovoltaic Specialists Conference*, Anchorage, AK, 15–22 September 2000, pp. 1242–1245.
- [20] S. Liu, R.A. Dougal, Dynamic multi-physics model for solar array, *IEEE Trans. Energy Convers.* 17 (2) (2002) 285–294.
- [21] B. Carpenter, J. Lyons, Lightweight Flexible Solar Array Experiment, NASA/GSFC EO-1 Technology Validation Report, 8 August 2001 (http://ldcm.usgs.gov/eo-1forum/Validation_Reports/LFSA.pdf).
- [22] B. Wu, R.E. White, Self-discharge model of a nickel-hydrogen cell, *J. Electrochem. Soc.* 147 (3) (2000) 902–909.
- [23] B. Wu, R.E. White, Modeling of a nickel–hydrogen cell, phase reaction in the nickel active material, *J. Electrochem. Soc.* 148 (6) (2001) 595–609.
- [24] M. Jain, A.L. Elmore, M.A. Mathews, J.W. Weidner, Thermodynamic consideration of the reversible potential for the nickel electrode, *Electrochem. Acta* 43 (18) (1998) 2649–2660.
- [25] S. Liu, R. Dougal, J. Weidner, L. Gao, Thermo-Electro-Chemical Model for Nickel Hydrogen Battery, submitted for publication.
- [26] R.D. Middlebrook, S.G. Kimble, Design of the HEAO main bus shunt regulator, *IEEE Trans. Aerospace Electron. Syst.* 12 (2) (1976) 162–172.
- [27] S. Kuwajima, T. Sato, N. Tsuya, M. Kobayashi, T. Okamura, Y. Honda, Digital sequential shunt regulator for solar power conditioning of Engineering Test Satellite (ETS-V), in: *Proceedings of the 19th Annual IEEE Power Electronics Specialists Conference*, vol. 2, 1988, pp. 619–625.
- [28] R.K. Barry, Conversion from full array shunt to partial shunt topology for two small explorer-class, near-earth orbiting scientific satellites, in: *Proceedings of the 31st Intersociety Energy Conversion Engineering Conference*, vol. 1, 1996, pp. 525–528.
- [29] P. Panneton, G. Dakermanji, D. Temkin, J. Jenkins, The preliminary design of the comet nucleus tour spacecraft power system, in: *Proceedings of the 35th Intersociety Energy Conversion Engineering Conference*, vol. 1, 2000, pp. 214–220.